

Available online at www.sciencedirect.com

ScienceDirect

www.elsevier.com/locate/jes

Research Article

Particle number size distributions and formation and growth rates of different new particle formation types of a megacity in China

Liang Dai¹, Yu Zhao^{1,2,*}, Lei Zhang¹, Dong Chen¹, Rongrong Wu¹¹ State Key Laboratory of Pollution Control and Resource Reuse and School of the Environment, Nanjing University, Jiangsu 210023, China² Jiangsu Collaborative Innovation Center of Atmospheric Environment and Equipment Technology (CICAET), Nanjing University of Information Science and Technology, Jiangsu 210044, China

ARTICLE INFO

Article history:

Received 19 April 2022

Revised 17 July 2022

Accepted 18 July 2022

Available online 27 July 2022

Keywords:

New particle formation

Size distribution

Formation and growth rate

Aerosol pollution

ABSTRACT

To understand the contribution of new particle formation (NPF) events to ambient fine particle pollution, measurements of particle size distributions, trace gases and meteorological conditions, were conducted at a suburban site (NJU) from October to December 2016 and at an industrial site (NUIST) from September to November 2015 in Nanjing. According to the temporal evolution of the particle size distributions, three types NPF events were observed: typical NPF (Type A), moderate NPF events (Type B) and strong NPF (Type C) events. The favorable conditions for Type A events included low relative humidity, low concentration of pre-existing particles, and high solar radiation. The favorable conditions of Type B events were similar to Type A, except for a higher concentration of pre-existing particles. Type C events were more likely to happen with the higher relative humidity, lower solar radiation and continuous growth of pre-existing particle concentration. The formation rate of 3 nm (J_3) was the lowest for Type A events and highest for Type C events. In contrast, the growth rates of 10 nm and 40 nm particles were the highest for Type A, and lowest for Type C. Results show that NPF events with only higher J_3 would lead to the accumulation of nucleation mode particles. Sulfuric acid was important for the formation of particles but had little effect on the growth of particle size.

© 2022 The Research Center for Eco-Environmental Sciences, Chinese Academy of Sciences. Published by Elsevier B.V.

Introduction

Airborne particles are ubiquitous in the atmosphere and directly or indirectly influence human lives (Wang et al., 2014b; Ye et al., 2017). For example, high particle exposure is

strongly associated with cardiovascular and respiratory diseases (Peng et al., 2017). As observed worldwide, new particle formation (NPF) significantly increases the number concentration of ambient submicron-size particles in the atmosphere (Wang et al., 2013a, 2014a; Salimi et al., 2015; Peng et al., 2017; Shang et al., 2018). The subsequent growth of newly formed particles affects atmospheric chemical processes and can lead to serious aerosol pollution (Ye et al., 2017; Yu et al., 2017).

* Corresponding author.

E-mail: yuzhao@nju.edu.cn (Y. Zhao).

In general, the particle size distribution can be divided into four modes: nucleation mode ($D_p < 20$ nm), Aitken mode (20 nm $< D_p < 100$ nm), accumulation mode (100 nm $< D_p < 1000$ nm) and coarse mode ($D_p > 1$ μ m) (Hussein et al., 2004). NPF events result in significant growth in the number concentration of nucleation mode particles (Lee et al., 2019), and the new particles can grow into Aitken mode particles, or even to the size of cloud condensation nuclei (CCN) (Cai et al., 2021). Sufficiently condensed vapors trigger nucleation and drive new particle growth (Merikanto et al., 2009). Sulfuric acid is considered a key compound in atmospheric nucleation (Sipila et al., 2010). Recent studies found that some organic oxidation products could accelerate the formation and growth rates of new particles (Metzger et al., 2010; Garmash et al., 2020). In addition, meteorological conditions may also influence new particle formation and subsequent growth. For example, Peng et al. (2017) found that the west wind was favorable for the formation of nucleation mode particles at Chang'an meteorological observation station in northwestern China. Interestingly, the east wind was favorable for the growth of nucleation mode particles.

In recent years, the rapid growth in industry and energy consumption has resulted in abundant emissions and thereby ambient concentrations of precursors for NPF. Various types of NPF events have been observed in China. A banana-shaped event is usually identified as a typical event (Kulmala et al., 2012), whereas other shapes (e.g., "apple" and "hump" shapes) indicate atypical events. Yu et al. (2019) found a type of atypical strong NPF event with a high formation rate and low growth rate at Xiangshan gulf of Zhejiang Province on the east coast of China. The formation rate of 2–7 nm particles and the growth rate of 7–20 nm particles were about 162 – 231 $\text{cm}^{-3} \text{sec}^{-1}$ and 4.4 nm/hr, respectively. They were respectively higher and lower than the average formation rate (~ 76 $\text{cm}^{-3} \text{sec}^{-1}$) and growth rate (~ 7.5 nm/hr) of the three urban agglomerations (the North China Plain, the Yangtze River Delta and the Pearl River Delta) in China (Zhang et al., 2021). The new particles did not increase in size and contributed little to the concentration of the Aitken mode particles. Peng et al. (2017) reported another type of atypical NPF event, in which the concentration of 50 nm particles increased slightly during the daytime.

The changing meteorological conditions could be the cause of different event types with varied particle formation and growth rates (Yu et al., 2016). For example, relatively high temperatures were conducive to the occurrence of typical NPF events (Peng et al., 2017). The average growth rate of typical events was 8 nm/hr, larger than that of atypical NPF events (~ 4.4 nm/hr). Approximately 60% of the apparent growth rate for typical events could be attributable to the condensation of sulfuric acid and its subsequent neutralization (Yue et al., 2010). There have been few comparative analyses of meteorological conditions, particle size distributions, particle formation and growth rates for different NPF event types in relatively polluted eastern China (Wang et al., 2014b; Qi et al., 2015; Shen et al., 2016). This limitation prevents a better understanding of the reasons and conditions for aerosol pollution formation in rapidly developing regions.

In this study, we selected Nanjing, a typical industrialized and economically developed city with relatively high aerosol

concentrations in East China, and conducted two campaigns on new particle formation and growth events at a suburban and an industrial site. Three types of NPF events were identified according to the temporal evolution of aerosol size distribution, and the favorable conditions for NPF events were derived through comparisons of the observed meteorological variables and diurnal patterns of trace gases and $\text{PM}_{2.5}$ levels by event type. Compared to our previous studies that conducted NPF event classification at a single site (Yu et al., 2016; Dai et al., 2017), we present the number concentrations of various particle modes by event type at both suburban and industrial sites in this work. We calculated and compared the formation and growth rate of particles for different event types. The possible mechanisms of particle nucleation were then analyzed based on the relationships between the calculated formation rates and the abundance of a proxy for sulfur acid, and the contributions of sulfuric acid to particle growth were quantified to reveal its varied roles in different event types.

1. Material and methods

1.1. Site descriptions

Two field campaigns were conducted at an industrial site (6 September–11 November 2015) and a suburban site (27 October–26 December 2016). As shown in Fig. 1, the industrial site is inside the campus of Nanjing University of Information Science & Technology (NUIST, 32.30°N , 118.72°E ; 60 m.a.g.l.) located downwind of Nanjing. The industrial facility cluster of the Nanjing Chemical Industry Park is 3 to 15 kilometers northeast of the site (An et al., 2015). The prevailing wind direction was easterly at the site during the campaign (see the joint probability plot in Fig. 1). NUIST was thus affected by industrial plumes from various petrochemical processes, such as smelting, petroleum refining and gas flaring at petrochemical facilities, containing SO_2 , NO_x , NH_3 , volatile organic compounds (VOCs), and amines (Zheng et al., 2015).

The suburban site is located on the roof of the School of the Environment building inside the Xianlin Campus of Nanjing University (NJU, 32.12°N , 118.95°E ; 30 m.a.g.l.), 20 km northeast of downtown Nanjing (Shen et al., 2018) (Fig. 1). During the campaign, the prevailing wind direction at the site was northeasterly (see the joint probability plot in Fig. 1). Few primary emission sources existed within a distance of 2–10 km around the site, and none were located upwind (Ding et al., 2013a). In contrast to NUIST, which was directly affected by local or nearby sources, NJU was affected by contaminants transported from longer distances. The site was expected to represent a regional background with low concentrations of gaseous pollutants (O_3 , SO_2 , and NO_2) (Ding et al., 2013a).

To further analyze the air pollutant sources affecting the two sites, we chose CO as a tracer, which has broad application prospects in understanding the origin and transport of air pollutants (Ding et al., 2013b). Nonparametric wind regression (NWR) was conducted for the measured CO during the campaigns (discussed in Section 2.2), as shown in Fig. 1. The NWR results exhibit distinct hot spots (higher concentrations) in the southeast wind sector of NUIST at wind speeds of approximately 0–6 km/hr and the southwest wind sector of NJU at

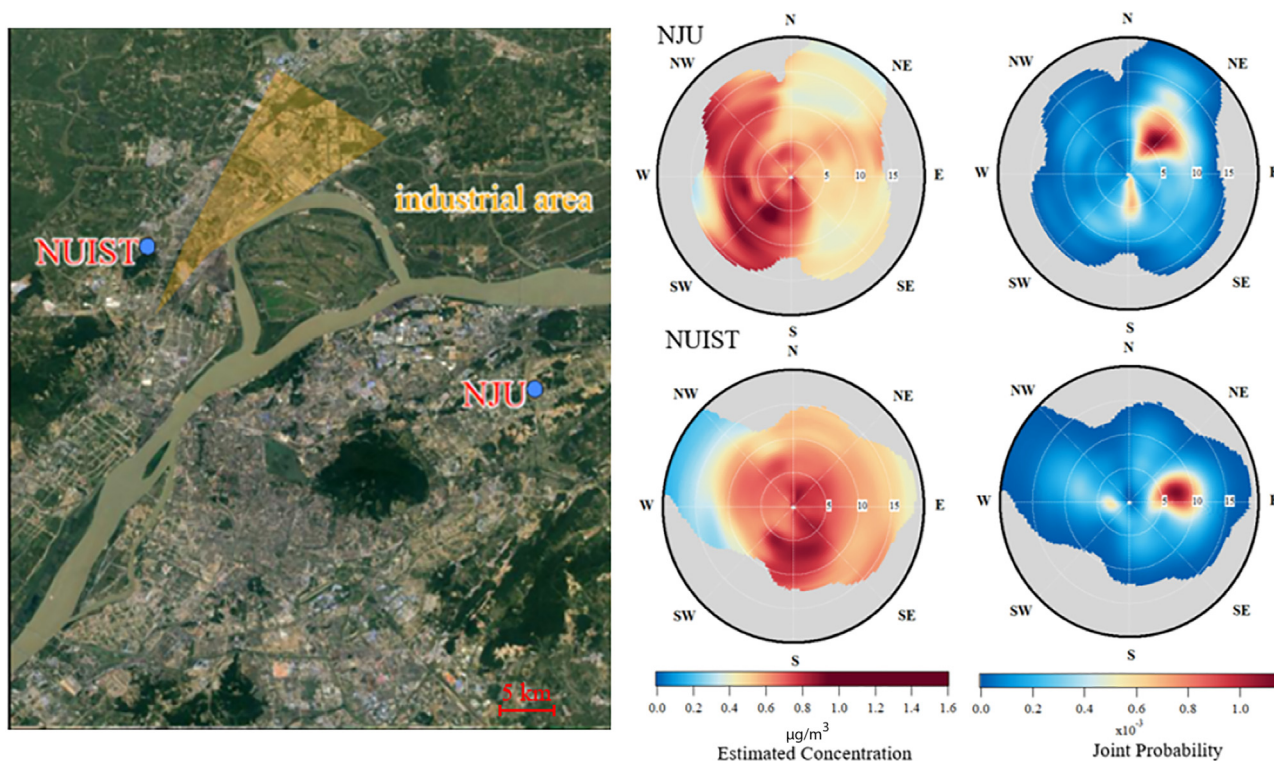


Fig. 1 – Locations of the suburban site (NJU) and industrial site (NUIST). Wind analysis results using nonparametric wind regression (NWR) of CO during the campaigns. Note: CO is a tracer of transport of air pollutants.

wind speeds of approximately 3–7 km/hr. This indicated that NUIST could be affected by pollutants emitted from the surrounding factories (Petit et al., 2017).

The meteorological fields during the research periods in 2015 and 2016 were compared for eastern China (29°N–33°N and 115°E–123°E) to evaluate the effect of the meteorological difference on the campaigns. The data were obtained from the European Centre for Medium-range Weather Forecasts (ECMWF) interim reanalysis (ERA-Interim) with a horizontal resolution at $0.25^\circ \times 0.25^\circ$. As shown in Table S1 in the supplementary material, good correlations were found for each meteorological factor between the two periods, with the correlation coefficients larger than 0.617. The comparison indicated that the uncertainty caused by the different meteorological condition was limited for the NPF measurements.

1.2. Instrumentation and classification of NPF events

The size distributions of particle number concentrations were measured at NUIST using a TSI Nano-SMPS (a differential mobility analyzer DMA3085 and a condensation particle counter CPC3776, TSI Inc., USA) with a scanning range of 3–160 nm and an MSP wide-range particle spectrometer (WPS XP-1000, MSP Corp., USA) with a scanning range of 10–10000 nm (Gao et al., 2009). The WPS system consists of a differential mobility analyzer (DMA) connected to a condensation particle counter (CPC) that measures 10–500 nm particles and to a laser particle spectrometer (LPS) that measures 350 nm–10 µm particles. The air sampling inlet was a 150-cm long and 1.0-cm inner diameter (ID), vertically oriented, stainless-steel tube with an airflow

of 5 standard liters per minute (sLpm). The transport loss of particles in the inlet was corrected using the size-dependent particle survival ratios calculated by a particle loss calculator tool (Weiden et al., 2009).

As SMPS could not be used due to instrumental maintenance in 2016, the more portable electrical aerosol spectrometer (EAS, Tartu University, Estonia) was applied at NJU to obtain the particle size distributions in the range from 3 to 10000 nm. EAS charges the particles and classifies them in a parallel multichannel mobility analyzer (MDMA) and measures the classified channel signals using an electrometric amplifier. The EAS consists of two multichannel mobility analyzer columns: the D-column measuring fine particles from 3 nm to 1 µm and the E-column measuring coarse particles from 300 nm to 10 µm. The particle size distributions are derived with a mathematical deconvolution procedure from the 20 D electrometers and the 20 E electrometers. The inlet was a 120-cm long and 3.0-cm ID, horizontally oriented, copper tube with an airflow of 30 sLpm. The transport loss of particles was corrected using the same method as that at NUIST.

The aerosol scanners were calibrated prior to campaigns and were properly maintained following the instructions of the instruments during the campaigns. Previous studies have indicated a good correlation between the data obtained by EAS and SMPS (Intra and Tippayawong, 2007; Mirme et al., 2007; Vana et al., 2016). Intra and Tippayawong (2007) pointed out that EAS number concentration was about 10% (range: 3%–15%) higher than that of SMPS in 5–1000 nm size range (Vana and Tamm, 2002). Therefore, the results measured by the two different scanners were believed to be comparable.

A gas chromatograph system (GC 5000; AMA Instruments GmbH, Germany) with a flame ionization detector (FID) was applied at NUIST to monitor the hourly concentration of 56 different ozone precursors specified by the US Environmental Protection Agency. The instrument was calibrated before monitoring (An et al., 2014). At NJU, a GC580 analysis system from PerkinElmer Instruments Clarus (Model-580, PerkinElmer, USA) was applied to conduct online VOC monitoring. The concentrations of TVOCs were obtained by summing the concentrations of the 56 VOC species. The time resolution of the GC at NJU was the same as that at NUIST. At both sites, the concentrations of SO₂, O₃, CO, and NO₂ were measured at a temporal resolution of 1 min using Thermo Environmental Instruments (Model 43i-TLE, 49i, 48i, and 42i, Thermo, USA). The PM_{2.5} concentration was monitored using a Thermo Scientific TEOM 1405 (Model-1405, Thermo, USA). During the campaigns, the two sites recorded meteorological parameters hourly, including wind speed, wind direction, relative humidity (RH), temperature and solar radiation from automatic weather stations (CSI-CR1000, Campbell, USA).

1.3. NPF classification

Particle growth after nucleation is crucial to determine whether new particles could grow to cloud-condensation-nuclei-active sizes. Based on the characteristics of the particle size spectrum, the classification of NPF events was conducted to explore the atmospheric conditions that were conducive to NPF. Dal Maso et al. (2005) divided the NPF events into 2 classes: Class I (typical events) and Class II (atypical events). Mazon et al. (2009) found that Class II could be further divided into a few sub-classes. For example, Hirsikko et al. (2007) expanded the number of classification types based on the difference in the charged nature of particles. Based on the particle size spectrum, other researchers divided Class II events into "bursting events", "hump events", "suppressed events", "stationary NPF events", or "weak NPF events" (Yli-Juuti et al., 2009; Vakkari et al., 2011; Chen et al., 2017; Dall'Osto et al., 2017; Groß et al., 2018; Lee et al., 2020).

To explore the effects of different event types on the particle number concentration, we classified the NPF event types with a refined strategy based on the criteria by Dal Maso et al. (2005). Fig. S1 in the supplementary material presents our refined decision tree for the event classification. Three NPF event types were divided according to the particle size spectrum: typical new particle formation events (light accumulation of number concentration of the nucleation mode particles, Type A), moderate accumulation of number concentration of the nucleation mode particles (Type B), and heavy accumulation of number concentration of the nucleation mode particles (Type C). There were similarities and differences between the event types of this study and Dal Maso et al. (2005). Type A events (typical events) corresponded to Class I: clear particle formation events, with little or no pre-existing particles obscuring the newly formed mode. A banana-shape growth was seen. Type B and C events (atypical events) were both violent NPF events and corresponded to part of Class II. The number concentration of nucleation mode particles increased sharply.

We distinguished Types B and C to evaluate the effect of atypical events on CCN. Particles with the size of 40–50 nm

could efficiently act as CCN (Casquero-Vera et al., 2020). In this work, the number concentration of 40–50 nm particles (N_{40-50}) increased by more than 1.5 times for Type B event, while the growth of N_{40-50} for Type C was less than 1.5 times. This indicated that Type B events could contribute more to CCN concentration than Type C (Yu et al., 2014).

1.4. Calculation of variables characterizing NPF

The event duration and stability of air mass are important for analyzing the particle formation and growth rates (Baalbaki et al., 2021; Qi et al., 2015). While the rationality was widely accepted for typical events (Type A), Baalbaki et al. (2021) pointed out that it was feasible to calculate the particle formation and growth rate of atypical events when the duration of these events was long enough (>15 min). As presented in Table 1, the durations of all the atypical (Type B and C) events were longer than 1 hour, thus the calculation of particle formation and growth rates is believed to be reasonable. Regarding the stability of air mass, we followed the method by Draxler and Rolph (2010) and illustrated the back trajectories during 48 hr by event type and site with the NOAA Hybrid Single-Particle Lagrangian Integrated Trajectory model (Fig. S2 in the Supplementary material). The trajectories were basically stable over large regions for all event types at both sites.

We used the general dynamic equation (GDE) to calculate particle growth and formation rates (Gelbard and Seinfeld, 1978; Kuang et al., 2012; Yu et al., 2016). Consistent with the high resolution of monitored data (4 min in this work), the method can reflect the rapid formation and growth rate of particles in the atmosphere. Details of the method have been described by Yu et al. (2016). The aerosol GDE describes the evolution of number concentrations in a size bin between particle diameters D_{p1} and D_{p2} ($D_{p2} > D_{p1}$):

$$\frac{dN(D_{p1}, D_{p2}, t)}{dt} = J(D_{p1}, t) - J(D_{p2}, t) - \text{coagSink}(D_{p1}, D_{p2}, t) + \text{coagSrc}(D_{p1}, D_{p2}, t) \quad (1)$$

where, $N(D_{p1}, D_{p2}, t)$ (cm^{-3}) is the particle number concentration in the size bin, inverted from the SMPS or EAS scanning data; J ($\text{cm}^{-3} \text{sec}^{-1}$) is the particle formation rate; and $\text{CoagSink}(D_{p1}, D_{p2}, t)$ and $\text{CoagSrc}(D_{p1}, D_{p2}, t)$ ($\text{cm}^{-3} \text{sec}^{-1}$) are the sink and source terms defining the coagulation out of and into the size bin between D_{p1} and D_{p2} , respectively. By assuming $J(50 \text{ nm}, t)$ in the largest size bin (i.e., the condensational growth flux out of 50 nm) to be negligible (Yu et al., 2016), we could calculate the formation rates $J(D_p, t)$ across all size bin boundaries. Once the formation rates $J(D_p, t)$ were obtained, the condensational growth rate $GR_{(D_p, t)}$ could then be calculated as $J_{(D_p, t)}/n_{(D_p, t)}$, where $n_{(D_p, t)}$ is the particle size distribution ($dN_{(p)}/dD_p$) for each size bin.

The condensational sink (CS) was calculated according to Dal Maso et al. (2005) and Ezhova et al. (2018). CS is an important parameter indicating the cleanliness of the atmosphere and can be calculated using Eq. (2) (An et al., 2015):

$$CS = 2\pi D_v \int_0^{D_{p,\max}} D_p \beta n(D_p) dD_p \quad (2)$$

where, D_v is the diffusion coefficient of the condensing vapors and $\beta = 3\alpha\beta_1/4Kn$. Here, Kn is the Knudsen number and calcu-

Table 1 – Summary of event type, date, duration, condensation sink (CS), average formation rate at 3 nm ($J_{3,ave}$) and 40 nm ($J_{40,ave}$), $J_{40,ave}/J_{3,ave}$, average growth rate at 10 nm ($GR_{10,ave}$), and average growth rate at 40 nm ($GR_{40,ave}$) at the suburban site (NJU) and industrial site (NUIST).

Site	Type	Date (mm/dd/year)	Duration (hr)	$J_{3,ave}$ ($cm^{-3} sec^{-1}$)	$J_{40,ave}$ ($cm^{-3} sec^{-1}$)	$J_{40,ave}/J_{3,ave}$	$GR_{10,ave}$ (nm/hr)	$GR_{40,ave}$ (nm/hr)	CS ($10^{-2} sec^{-1}$)
NJU	A	10/30/2016	3.07	9.45	0.39	0.041	14.31	6.46	1.01 ± 0.08
NJU	A	11/8/2016	4.07	6.35	0.39	0.061	11.02	6.82	1.00 ± 0.10
NJU	A	11/15/2016	4.53	7.40	0.65	0.088	20.28	5.91	1.28 ± 0.45
NJU	A	12/2/2016	3.67	6.44	0.51	0.079	12.32	13.8	1.22 ± 0.42
NJU	B	11/1/2016	3.93	12.71	0.78	0.061	12.16	6.57	1.03 ± 0.18
NJU	B	11/4/2016	4.07	12.88	0.79	0.061	18.88	6.69	1.06 ± 0.24
NJU	B	12/6/2016	4.87	9.37	0.58	0.062	-	6.43	1.53 ± 0.61
NJU	B	12/8/2016	4.47	12.20	0.50	0.041	15.62	7.35	1.55 ± 0.74
NJU	B	12/16/2016	2.67	18.43	0.39	0.021	9.19	10.21	1.54 ± 0.71
NJU	B	12/23/2016	3.07	8.38	0.21	0.025	11.24	6.83	1.62 ± 0.60
NJU	C	10/31/2016	5.33	15.36	0.23	0.015	-	4.54	1.64 ± 0.35
NJU	C	11/21/2016	5.87	9.54	0.16	0.017	-	4.19	1.42 ± 0.50
NJU	C	11/27/2016	9.2	20.44	0.42	0.021	8.59	6.70	2.10 ± 0.30
NJU	C	12/7/2016	4.27	14.31	0.22	0.015	18.49	5.61	-
NJU	C	12/10/2016	5.53	9.79	0.21	0.021	7.16	4.51	1.98 ± 0.27
NUIST	A	9/14/2015	3.47	3.60	0.17	0.047	18.23	2.93	-
NUIST	A	9/20/2015	2.67	6.92	0.66	0.095	25.00	10.25	1.12±0.32
NUIST	A	10/1/2015	1.67	7.14	0.35	0.049	41.20	5.62	1.11±0.31
NUIST	A	10/2/2015	1.8	5.98	0.15	0.025	5.39	4.31	1.34±0.49
NUIST	A	10/10/2015	1.4	4.37	0.21	0.048	29.19	3.65	1.69±0.46
NUIST	A	10/11/2015	3.27	3.08	0.12	0.039	40.72	6.12	1.08±0.27
NUIST	A	10/18/2015	1.8	7.98	0.43	0.054	20.82	6.13	1.73±0.52
NUIST	A	10/27/2015	3.27	3.77	0.15	0.040	9.27	3.29	1.03±0.28
NUIST	A	10/31/2015	1.8	3.49	0.36	0.103	5.52	3.98	1.03±0.17
NUIST	A	11/1/2015	1.93	2.59	0.22	0.085	16.69	2.78	1.43±0.50
NUIST	B	9/13/2015	1.8	8.65	0.53	0.061	12.52	2.14	-
NUIST	B	9/27/2015	5.4	10.76	0.83	0.077	17.19	6.91	1.32 ± 0.52
NUIST	B	10/12/2015	3.73	7.98	0.19	0.024	16.02	2.81	1.00 ± 0.10
NUIST	B	10/30/2015	4.33	13.01	0.40	0.031	3.60	2.13	1.16 ± 0.37
NUIST	C	9/24/2015	5.73	41.23	0.21	0.005	13.13	2.76	1.40 ± 0.56
NUIST	C	9/26/2015	4.8	22.17	0.04	0.002	3.38	2.89	1.31 ± 0.47
NUIST	C	9/28/2015	4.6	16.76	0.12	0.007	11.46	2.77	1.50 ± 0.10

lated as $2\lambda/D_p$, where λ (nm) is the mean free path of condensing molecules.

Sulfuric acid is believed to play an important role in NPF (Kulmala, 2013). For long-term observation, the daytime sulfuric acid concentration was calculated using a proxy method (Kurten et al., 2016):

$$[H_2SO_4]_{proxy} = \alpha \times k(T, p) \times [SO_2]^b \times Rad^c \times RH^d \times CS^e \quad (3)$$

where, k is a rate constant dependent on ambient temperature T (K) and pressure p (Pa) (Mikkonen et al., 2011), $[SO_2]$ is the mixing ratio (ppbv), Rad is the radiation (W/m^2), RH is the relative humidity (%), and CS is the condensation sink (sec^{-1}). The performance of a proxy equation is site-specific due to varying atmospheric conditions from one site to another (Lu et al., 2019). Yao et al. (2018) parameterized the proxy equation proposed by Mikkonen et al. (2011) based on measurements in Shanghai, which is geographically close to Nanjing and shares similar atmospheric conditions with Nanjing. The coefficients a , b , c , d , and e were 1.321×10^{15} , 0.913, 0.990, -0.217 and -0.526 , respectively (Yao et al., 2018). The concentrations of SO_2 , NO_2 , CO , O_3 and CS in Nanjing were 7.3–16.2, 22.69–40.06, 790–960, 42–76 $\mu g/m^3$ and 0.018–0.026 sec^{-1} , while those in Shanghai were 3–15, 20–70, 300–900, and 20–50 $\mu g/m^3$

and 0.007–0.030 sec^{-1} , respectively. As the pollutant concentrations and CS during our observation period were in similar ranges with those of Yao et al. (2018). Thus, we believed that the new parameterized proxy equation could be applied to Nanjing.

The contribution of sulfuric acid to the growth rate needed to be estimated to evaluate the contribution of other substances. We calculated the sulfuric acid vapor concentration required for a growth rate of 1 nm/hr over a range of particle sizes based on Nieminen et al. (2010):

$$C_{GR=1nm/hr} = \frac{2\rho_v d_v}{\gamma m_v \Delta t} \sqrt{\frac{\pi m_v}{8kT}} \left[\frac{2x_1 + 1}{x_1(x_1 + 1)} - \frac{2x_0 + 1}{x_0(x_0 + 1)} + 2 \ln \frac{x_1(x_0 + 1)}{x_0(x_1 + 1)} \right] \quad (4)$$

where, x_0 and x_1 are the ratios of the diameter of the vapor molecule (d_v) to the diameter of the initial particle and grown particle, respectively. The mass (m_v) and density (ρ_v) of sulfuric acid applied in this study are 135 amu and 1650 kg/m^3 , respectively, corresponding to sulfuric acid molecules (Kurten et al., 2007). However, $C_{GR=1nm/hr}$ could possibly be underestimated because the efficiency of the adhesion of sulfuric acid molecules to particles may not reach 1.

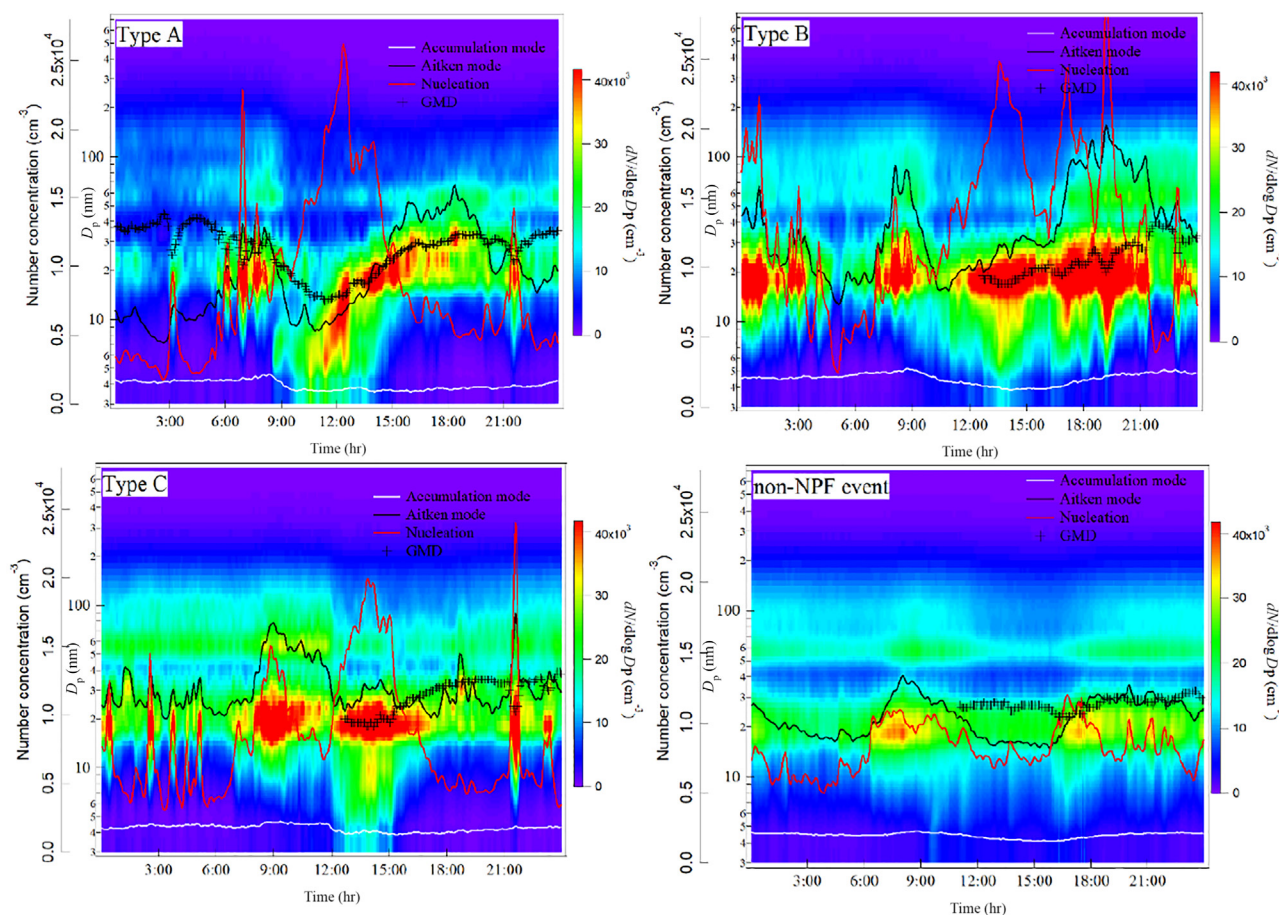


Fig. 2 – Time series for average particle size distributions for NPF (Type A, B and C) and non-NPF events at NJU. The nucleation (red line), Aitken (black line) and accumulation (white line) mode concentrations and the particle geometric mean diameter (GMD, plus signs) are shown.

The growth rate related to sulfuric acid condensation ($GR_{H_2SO_4}$) (Wang et al., 2015) was then calculated using Eq. (5):

$$GR_{H_2SO_4} = [H_2SO_4] / C_{GR=1nm/hr, H_2SO_4} \quad (5)$$

where, $[H_2SO_4]$ is the concentration of sulfuric acid. Since we did not directly measure the concentration of sulfuric acid in the atmosphere, we used $[H_2SO_4]_{proxy}$ calculated with Eq. (3).

2. Results and discussion

2.1. Particle size distributions for different NPF event types

According to the classification strategy described in Section 2.3, 4 Type A, 6 Type B and 5 Type C events were identified among the 59 observation days at NJU, while 10 Type A, 4 Type B and 3 Type C events were identified among the 55 observation days at NUIST, as summarized in Table 1. The occurrence frequency of NPF events at NJU was 25% and 31% at NUIST during the entire campaign.

Figs. 2 and 3 illustrate the averaged diurnal variations in particle size distributions for Type A, B and C events and non-

NPF events at NJU and NUIST, respectively. It should be noted that the particles were relatively large when they first appeared, resulting from the NPF events transported from other regions or changed emissions at night. On one hand, the NPF events could occur at night in other areas, and the grown particles were brought to the site by air mass. On the other hand, the emissions of motor vehicles could result in abundant particles with a size of 15–25 nm. The situation was particularly obvious at NJU, as it is close to a highway which heavy-duty vehicles are allowed to pass at night. During the daytime, the concentration of those particles would decrease rapidly through the movement of the airflow and the rise of the boundary layer height.

The increase in number concentration of nucleation mode particles for NPF events could not be induced by plume nucleation. The plume nucleation would rapidly elevate the number concentration of nucleation mode particles within a very short time, and the number concentration of particles in atmosphere would decline afterwards. During the daytime of NPF events, in contrast, the number concentration of nucleation mode particles maintained a high concentration for a long time (>1 hr), thus they were not plume events. For the non-NPF days, although the number concentration of nucleation mode particles increased, the subsequent growth of the

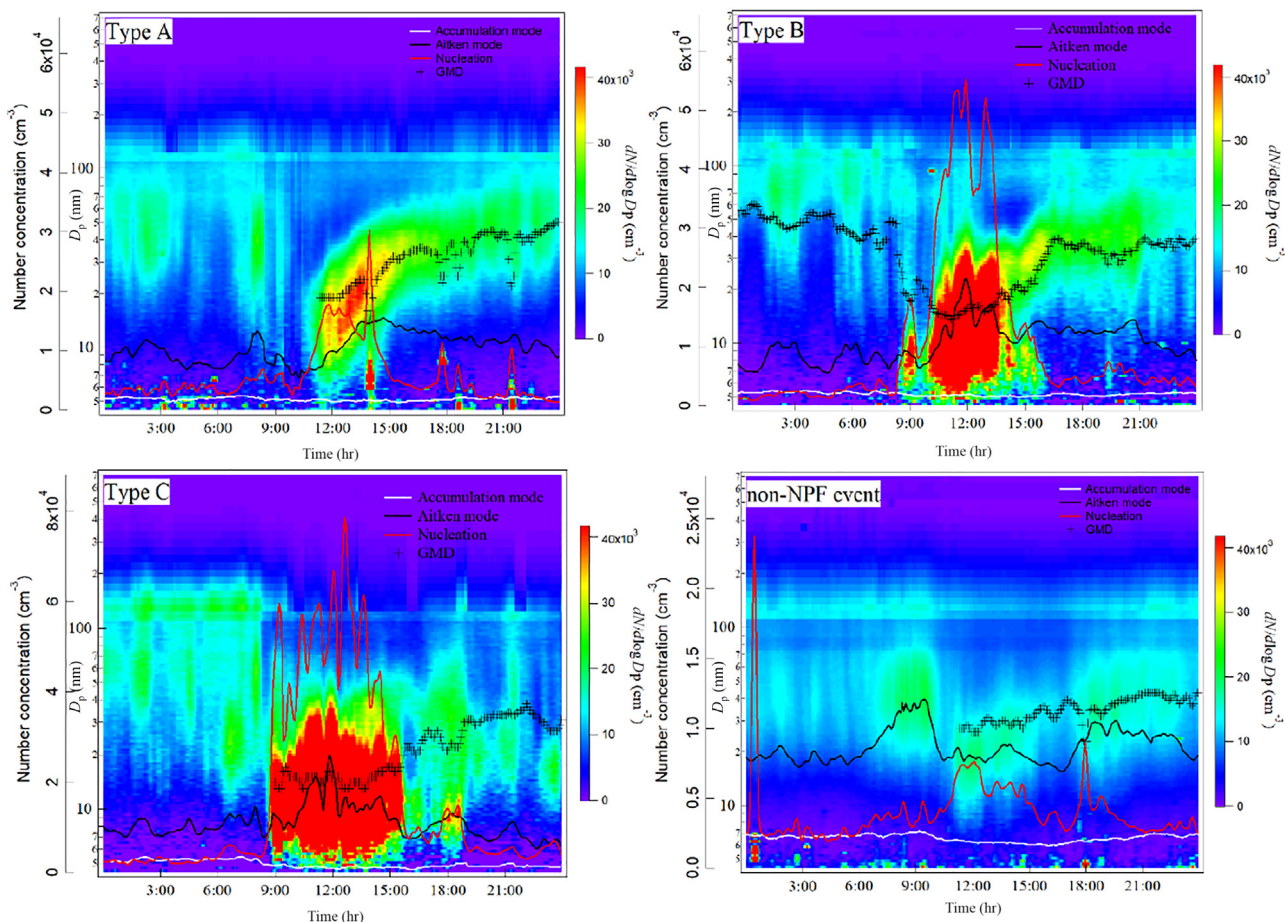


Fig. 3 – Time series for average particle size distributions for NPF (Type A, B and C) and non-NPF events at NUIST. The nucleation (red line), Aitken (black line) and accumulation (white line) mode concentrations and the particle geometric mean diameter (GMD, plus signs) are shown. Please note the different scale for the y axis for number concentration.

number concentration of Aitken mode particles did not appear. The duration of nucleation mode particles was relatively short (<1 hr).

Fig. S3 shows the contour plot of particle number size distribution for different event types at NJU and NUIST. The contours of particle number size distribution for Type A were uniform distribution banana shapes. The contours of particle number size distribution for Type B were uneven distribution banana shapes. However, there were no banana shapes for the contours of particle number size distribution for Type C at NJU and NUIST. It indicates that part of new particles can keep grow up, like Type A events, during Type B events.

More serious accumulation of nucleation mode particles was clearly found in Type C events compared with Type A. Table 2 summarizes the average particle number concentrations of different modes for different event types at the two sites. The total average number concentrations ranked in the order of Type C $(3.4 \pm 1.7) \times 10^4 \text{ cm}^{-3}$ at NJU and $(6.6 \pm 3.3) \times 10^4 \text{ cm}^{-3}$ at NUIST) > Type B $(3.3 \pm 1.2) \times 10^4 \text{ cm}^{-3}$ at NJU and $(5.5 \pm 3.8) \times 10^4 \text{ cm}^{-3}$ at NUIST) > Type A events $(2.8 \pm 1.7) \times 10^4 \text{ cm}^{-3}$ at NJU and $(2.4 \pm 1.3) \times 10^4 \text{ cm}^{-3}$ at NUIST). The average number concentrations of the nucleation mode (3–20 nm)

Table 2 – Average particle number concentrations of different modes for different NPF event types at the two sites.

	Type	Nucleation mode	Aitken mode	Total
NJU (10^4 cm^{-3})	A	1.9 ± 1.7	0.9 ± 0.5	2.8 ± 1.7
	B	2.1 ± 1.2	1.2 ± 0.4	3.3 ± 1.2
	C	2.0 ± 1.7	1.3 ± 0.5	3.4 ± 1.7
NUIST (10^4 cm^{-3})	A	1.4 ± 1.3	1.0 ± 0.6	2.4 ± 1.3
	B	4.3 ± 3.8	1.2 ± 0.6	5.5 ± 3.8
	C	5.1 ± 3.2	1.5 ± 3.2	6.6 ± 3.3

and Aitken mode (20–100 nm) particles were $(1.9 \pm 1.7) \times 10^4$ and $(0.9 \pm 0.5) \times 10^4$, $(2.1 \pm 1.2) \times 10^4$ and $(1.2 \pm 0.4) \times 10^4$, and $(2.0 \pm 1.7) \times 10^4$ and $(1.3 \pm 0.5) \times 10^4 \text{ cm}^{-3}$ during Type A, B, and C events at NJU, respectively; while the analogs at NUIST were $(1.4 \pm 1.3) \times 10^4$ and $(1.0 \pm 0.6) \times 10^4$, $(4.3 \pm 3.8) \times 10^4$ and $(1.2 \pm 0.6) \times 10^4$, and $(5.1 \pm 3.2) \times 10^4$ and $(1.5 \pm 3.2) \times 10^4 \text{ cm}^{-3}$, respectively (Table 2). In general, the concentrations of nucleation mode (3–20 nm) and Aitken mode (20–100 nm) particles in Type A events were the lowest among all event types.

Aitken mode particles are generated from the growth of nucleation mode particles. Before the NPF events started, the average fractions of Aitken mode particles were lowest in Type A events (27.7% for NUIST and 42.3% for NJU). During NPF events, the average number concentrations of Aitken mode particles accounted for 55.5%, 42.4% and 36.9% of the total number concentrations in Type A, B and C events at NUIST, respectively, and 45.7%, 39.2%, and 40.6% at NJU, respectively. The growth of Aitken mode particles during Type A events (particularly at NUIST) implied the more important role of typical NPF on the particle concentration compared with the other two types.

The initial geometric mean diameters (GMD) of the particles (3 nm–10,000 nm) were 15, 15, and 20 nm for Type A, B and C events at NJU, respectively, and 20, 15 and 15 nm at NUIST, respectively. They were observed to grow to 40, 35, and 35 nm during Type A, B and C events at NJU, and 50, 40, and 30 nm at NUIST, respectively. The largest growth in GMD was found for Type A events and the smallest for Type C events, resulting possibly from the changed CS for different event types. Table 1 summarizes the main variables for different event types during the campaigns. The average CS during Type A, B and C events were 0.011 ± 0.0014 , 0.014 ± 0.0027 , and $0.018 \pm 0.0031 \text{ sec}^{-1}$ at NJU, and 0.013 ± 0.0028 , 0.012 ± 0.0016 , and $0.014 \pm 0.0010 \text{ sec}^{-1}$ at NUIST, respectively. The lowest and highest average CS were found for Type A and C events, respectively. The lifetimes of molecular clusters and gas-phase, low-volatility compounds were inversely proportional to the CS. The high CS limited the concentrations of low-volatility compounds and in turn restrained the particle growth.

Fig. 4a and c demonstrate that the size distributions of surface area concentrations were bimodal with peaks at 100–200 nm and 1.0–2.0 μm at NJU and trimodal with peaks at 100–200 nm, 500–600 nm and 1.0–1.5 μm at NUIST. Regardless of the event type, the particles with a size range of 0.2–2.0 μm greatly contributed to the surface area concentrations. Fig. 4b and d show bimodal size distributions of aerosol number concentrations for all event types. For Type A, B, and C events at NJU, the first peak of aerosol number concentrations was at 20–30 nm, 10–20 nm, and 10–15 nm, and the second was at 800–900 nm, 1.0–1.5 μm , and 1.0–1.5 μm , respectively (Fig. 4b). At NUIST, the first peak was at 25–45 nm, 10–30 nm, and 10–15 nm for Type A, B, and C events, respectively, while the second was at 400–600 nm for all event types (Fig. 4d). For Type A, B and C events, the position of the first peak moved to a smaller particle size, and the peak concentration of particle numbers was elevated. The geometric standard deviation (σ_g) for the nucleation mode, which could be elevated by intense growth of nucleation mode particles (Alonso-Blanco et al., 2018), was largest during Type A events at both sites (2.51 for NJU and 5.01 for NUIST). These results confirmed that the strongest particle growth occurred in Type A events.

2.2. Variations in trace gases, $\text{PM}_{2.5}$ and meteorological variables by event types

Table 3 summarizes the average concentrations of trace gases and $\text{PM}_{2.5}$ during the daytime for different NPF event types at the two sites. Clearly, higher concentrations of SO_2 , NO_2 and TVOCs were found at NUIST, implying the influence of the sur-

rounding industrial factories on the site. The lowest concentrations were observed during Type A events at both sites for all species except O_3 .

As shown in Figs. S4 and S5 in the supplementary material, the average diurnal variations in trace gases largely changed for different event types. O_3 exhibited unimodal distributions, and peaks appeared at 12:00 when the concentrations of nucleation mode particles were highest at both sites. Sufficient photochemical products were conducive to the formation and growth of particles. The average O_3 concentration was highest for Type A events ($105.21 \pm 23.64 \mu\text{g}/\text{m}^3$ at NJU and $84.92 \pm 44.68 \mu\text{g}/\text{m}^3$ at NUIST) and lowest for Type C events ($56.09 \pm 37.21 \mu\text{g}/\text{m}^3$ at NJU and $55.54 \pm 30.76 \mu\text{g}/\text{m}^3$ at NUIST, Table 3), while the average concentration of TVOCs was lowest for Type A and highest for Type C (Fig. S6). The growth of particles was limited by the photochemical products related to O_3 (Wang et al., 2015). The lack of photochemical products, indicated by lower O_3 , limited the particle growth for atypical NPF events, thus the continuous banana-shaped growth did not take place (Types B and C) (Palm et al., 2017). Bimodal diurnal variations were observed for CO and NO_2 , with two peaks at 06:00–09:00 and 17:00–20:00, consistent with rush hour traffic. The concentrations of CO and NO_2 in Type A events were lower than those in Type B and C events, indicating that Type A events could occur in conditions with less human interference. Unimodal diurnal variations were observed for SO_2 , with peaks at 8:00–10:00 at both sites. The relatively similar SO_2 concentrations for all event types implied that SO_2 was not a key factor differentiating the event types.

Pre-existing particulate matter ($\text{PM}_{2.5}$) in the atmosphere scavenges the condensable gases and thus reduces their concentrations (Kanawade et al., 2012). As shown in Figs. S4 and S5, the diurnal variations in $\text{PM}_{2.5}$ were consistent in the same event types at both sites. The $\text{PM}_{2.5}$ concentration was lowest with weak diurnal variation in Type A events, and it was favorable for the growth in particle size. In Type B events, the maximum and minimum concentrations were found at 9:00 and 12:00, respectively. Moreover, a continuous growth pattern was found in Type C events during daytime. This growth was expected to reduce the condensable gas levels and to prevent particle growth.

As shown in Fig. 5, similar diurnal patterns of meteorological variables were found at both sites. All the meteorological variables were recorded by automatic weather station (CSI-CR1000, Campbell, USA) at both sites. For Type A, B and C events, the mean values of RH at NJU and NUIST were 53.8% and 60.7%, 54.3% and 62.0%, and 73.3% and 73.1%, respectively. The mean values of temperature at the two sites were 9.4°C and 24.8°C, 11.0°C and 25.5°C, and 12.2°C and 30.1°C, respectively. The mean values of solar radiation flux at the two sites were 276.6 W/m^2 and 487.3 W/m^2 , 316.6 W/m^2 and 504.0 W/m^2 , and 160.7 W/m^2 and 372.5 W/m^2 , respectively. The meteorological conditions during Type A events were generally more favorable in aiding particle formation and growth than those during Type B or C events: lower RH, lower temperature, and higher solar radiation flux. The favorable meteorological conditions of Type A events are roughly consistent with a previous study (Kanawade et al., 2012). Low RH is associated with strong radiation, and they accelerate the photochemical production of the precursors favorable for new particle formation

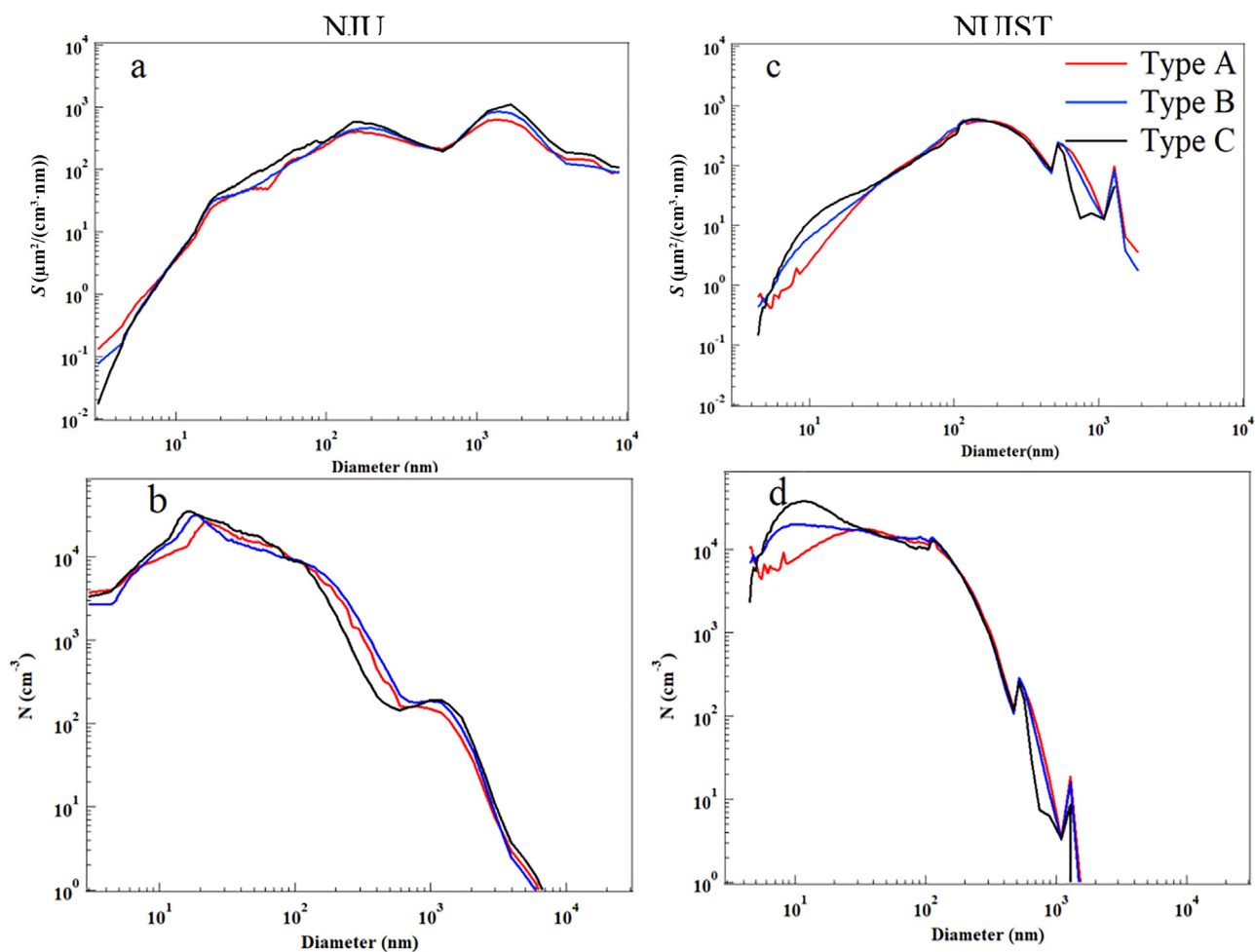


Fig. 4 – Size distributions of surface area concentrations (a and c) and aerosol number concentrations (b and d) under different event types at NJU (left panel) and NUIST (right panel).

Table 3 – Average concentrations of trace gas and $\text{PM}_{2.5}$ during the daytime for different NPF event types at the two sites.

Type	$\text{PM}_{2.5}$ ($\mu\text{g}/\text{m}^3$)	SO_2 ($\mu\text{g}/\text{m}^3$)	NO_2 ($\mu\text{g}/\text{m}^3$)	O_3 ($\mu\text{g}/\text{m}^3$)	TVOCs (ppbv)	
NJU	A	30.92 ± 13.28	7.66 ± 2.44	11.78 ± 3.44	105.21 ± 23.64	2.95 ± 2.54
	B	39.93 ± 22.41	9.50 ± 4.95	14.55 ± 3.99	81.33 ± 34.27	7.22 ± 7.08
	C	39.61 ± 29.21	8.48 ± 3.24	20.46 ± 4.60	56.09 ± 37.21	7.68 ± 5.78
NUIST	A	30.80 ± 17.14	13.28 ± 7.94	26.94 ± 16.13	84.92 ± 44.68	12.84 ± 8.72
	B	33.10 ± 15.38	17.79 ± 6.15	28.42 ± 15.14	81.78 ± 53.28	13.42 ± 4.94
	C	32.82 ± 15.04	13.97 ± 4.46	31.1 ± 13.91	55.54 ± 30.76	18.00 ± 7.00

(e.g., sulfuric acid, Mikkonen et al., 2011). Low temperature facilitated the condensation of low-volatility gases on new particles, which was conducive to the growth in particle size. As a result, continuous banana-shaped particle growth was observed during the Type A events.

In summary, the favorable conditions for Type A events included low relative humidity, low concentrations of pre-existing particles, and high solar radiation. The favorable conditions of Type B events were similar with to Type A, except for a higher concentration of pre-existing particles. The favorable conditions for Type C events were opposite to that of Type A,

with a continuous growth of pre-existing particle concentration.

2.3. New particle formation event analysis

2.3.1. Characteristics of the formation and growth rate of particles during NPF events

The NPF events were found to start from sizes close to 3 nm and ended with the size ranging from 40 nm to 50 nm at both sites. Five size bins of 3–10, 10–20, 20–30, 30–40, and 40–50 nm were defined for the size distributions of particle number con-

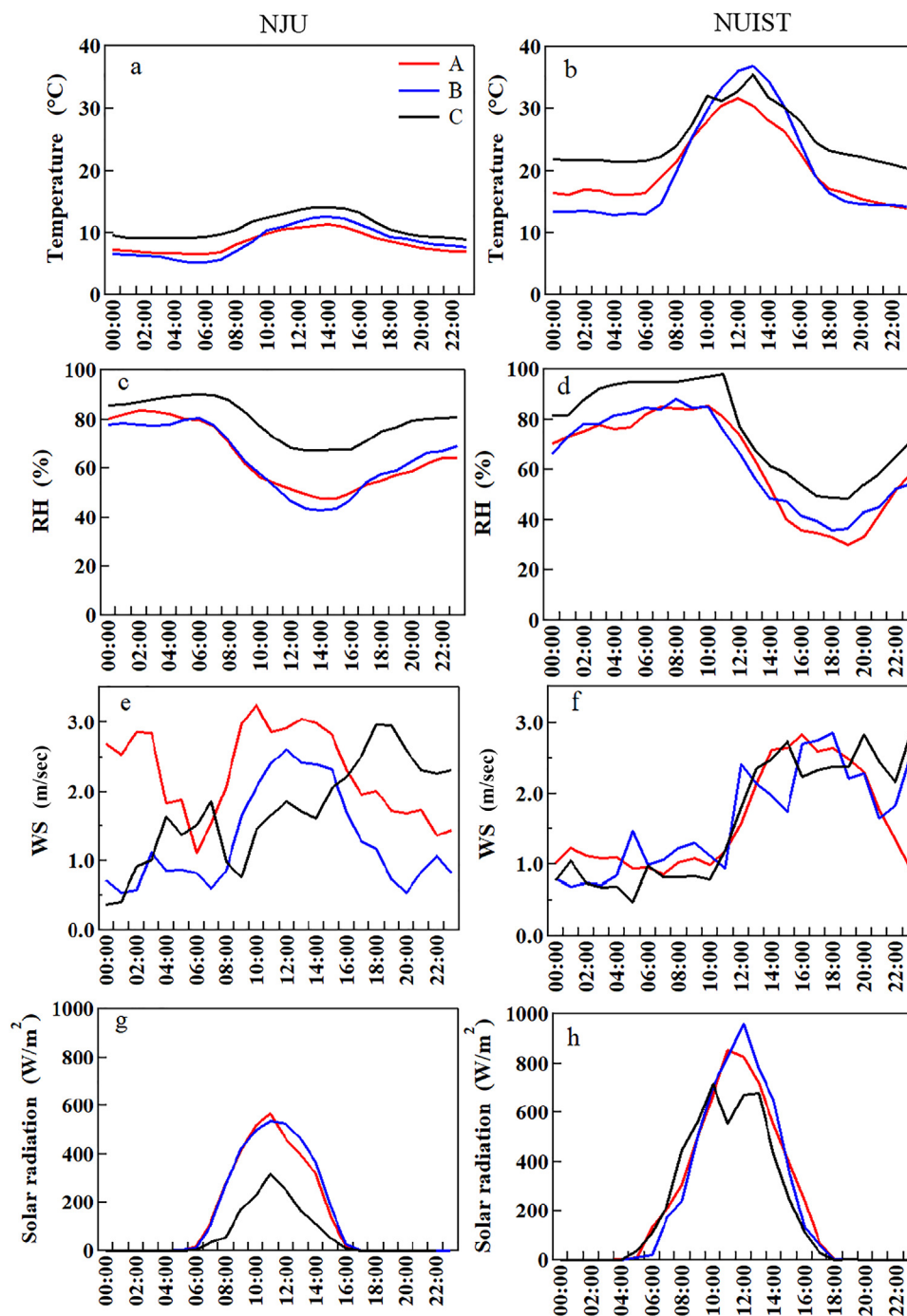


Fig. 5 – Diurnal variations in meteorological elements (temperature (a and b), RH (c and d), wind speed (e and f) and solar radiation flux (g and h)) for different event types at NJU (left panel) and NUIST (right panel).

concentrations at both sites. Based on the GDE method, we obtained $J_{(3\text{ nm}, t)}$, $J_{(40\text{ nm}, t)}$, $\text{GR}_{(10\text{ nm}, t)}$ and $\text{GR}_{(40\text{ nm}, t)}$ (hereafter J_3 , J_{10} , GR_{10} , and GR_{40}). The formation rate (J) and growth rate (GR) of particles are important parameters that characterize the observed NPF events. They directly affect the number concentration of ambient particles. As summarized in Table 1, $J_{3,\text{ave}}$ was highest during Type C events ($13.9 \pm 4.5\text{ cm}^{-3}\text{ sec}^{-1}$ at NJU and $26.7 \pm 12.8\text{ cm}^{-3}\text{ sec}^{-1}$ at NUIST), moderate during Type B events ($12.3 \pm 3.5\text{ cm}^{-3}\text{ sec}^{-1}$ at NJU and $10.1 \pm 2.7\text{ cm}^{-3}\text{ sec}^{-1}$ at

NUIST) and lowest during Type A events ($7.4 \pm 1.4\text{ cm}^{-3}\text{ sec}^{-1}$ at NJU and $4.9 \pm 1.9\text{ cm}^{-3}\text{ sec}^{-1}$ at NUIST), i.e., 3 nm particles formed fastest during Type C events but slowest during Type A events.

The formation rate of particles with different diameters could affect the particle size spectrum shape. $N(D_3, D_{40}, t)$, $\text{CoagSnk}(D_3, D_{40}, t)$ and $\text{CoagSrc}(D_3, D_{40}, t)$ depended on time. Compare with $N(D_3, D_{40}, t)$, the values of $\text{CoagSnk}(D_3, D_{40}, t)$ and $\text{CoagSrc}(D_3, D_{40}, t)$ were relatively small, and Eq. (1) can

be written as $N_{(D3, D40, t)} \approx J_{(3, t)} \cdot J_{(40, t)}$. We defined the ratio of $J_{40,ave}/J_{3,ave}$ to reflect the variation of number concentration of small particles ($D_p < 40$ nm). A higher ratio suggested a weaker accumulation of small particles and thereby a low number concentration of particles in the size bin of 3–40 nm. We found that the average $J_{40,ave}/J_{3,ave}$ was highest during Type A events (0.065 and 0.057 at NJU and NUIST, respectively), moderate during Type B events (0.044 and 0.048 at NJU and NUIST, respectively) and lowest during Type C events (0.018 and 0.005 at NJU and NUIST, respectively). The results thus indicated that the occurrence of Type C events was related to the accumulation of small particles, as shown in Fig. 4b and d.

$GR_{10,ave}$ and $GR_{40,ave}$ were calculated at 14.5 ± 4.1 and 8.2 ± 3.7 nm/hr during Type A events, 13.4 ± 3.8 and 7.4 ± 1.4 nm/hr during Type B events, and 11.4 ± 6.2 and 5.1 ± 1.0 nm/hr during Type C events at NJU, respectively. The analogs at NUIST were 21.2 ± 13.0 and 4.9 ± 2.3 nm/hr, 12.3 ± 6.2 and 3.5 ± 2.3 nm/hr, and 9.3 ± 5.2 and 2.8 ± 0.1 nm/hr, respectively (Table 1). The factors that affect the growth of particles include gaseous precursors (e.g., H_2SO_4 and highly oxygenated organic molecules) and pre-existing aerosols in the atmosphere (e.g., $PM_{2.5}$). When there were sufficient pre-existing large particles, the gaseous precursors in the atmosphere tended to accumulate on the surface of the large particles (Anttila et al., 2010). In addition, the collision of small particles ($D_p < 40$ nm) on the surface of large particles could reduce their concentrations (Kerminen et al., 2001). As shown in Table S2 in the supplementary material, the average $PM_{2.5}$ concentrations during Type A events were lowest (28.1 and $28.5 \mu\text{g}/\text{m}^3$ at NJU and NUIST, respectively). The nucleation mode particles were thus more likely to grow in size than those during Type B and C events. As discussed in Section 2.1, the distinctly elevated average fractions of Aitken mode particles may due to the higher GR_s for Type A events.

2.3.2. Relationship between sulfuric acid and particle formation and growth rates

Fig. 6 illustrates the correlations between J_3 and the calculated sulfuric acid concentrations for different event types at NUIST and NJU. J_3 was found to be positively correlated with the sulfuric acid proxy in Type A and Type B events, with slopes of $\log J_3$ versus $\log[H_2SO_{4,proxy}]$ close to 1 at NJU and NUIST. The slopes of $\log J_3$ vs. $\log[H_2SO_{4,proxy}]$ were close to 0.5 for Type C events at both sites. Previous studies have pointed out that the nucleation rate was proportional to the first or second power of the concentration of gas-phase sulfuric acid, i.e., $J = A \cdot [H_2SO_4]^P$, where P was equal to 1 or 2, conventionally interpreted as the number of sulfuric acid molecules in the critical nucleus, and A was a pre-exponential factor (Sihto et al., 2009; Xiao et al., 2015). The slopes of $\log J_3$ versus $\log[H_2SO_{4,proxy}]$ for Type A and B events were close to 1, implying collision limited nucleation (Sipila et al., 2010; Wang et al., 2011). The slopes of Type C were proportional to the power of the sulfuric acid proxy of approximately 0.5, suggesting that Type C events could be explained by activation nucleation (Xiao et al., 2015). We found that the formation rate of Type C events was fastest under the same sulfuric acid concentration. Thus, other precursors (e.g., amines) combine with sulfuric acid to reduce the energy barrier prior to spontaneous transformation from

gaseous to particle phase in Type C events (Xiao et al., 2015; Zhang et al., 2015).

A recent study found that anthropogenic aromatics photooxidation would accelerate the formation or growth of particles, with or without H_2SO_4 (Metzger et al., 2010). Fig. S6 in the supplementary material shows the concentrations of sulfuric acid proxy and TVOCs of different types of events at the two sites. The average concentration of sulfuric acid was highest of Type A events (3.54 ± 2.56) $\times 10^6 \text{ cm}^{-3}$ at NJU and (2.92 ± 2.04) $\times 10^6 \text{ cm}^{-3}$ at NUIST), moderate of Type B events (3.49 ± 2.54) $\times 10^6 \text{ cm}^{-3}$ at NJU and (2.52 ± 1.70) $\times 10^6 \text{ cm}^{-3}$ at NUIST) and lowest of Type C events (1.83 ± 2.06) $\times 10^6 \text{ cm}^{-3}$ at NJU and (1.67 ± 1.36) $\times 10^6 \text{ cm}^{-3}$ at NUIST). In contrast, the highest average concentration of TVOCs was found for Type C events and the lowest for Type A events. The pattern for $J_{3,ave}$ was consistent with that of TVOCs. TVOCs can be an indicator of organic amines and highly oxygenated molecules (HOMs), thus the highest TVOCs level for Type C events indicated that those compositions could be potential drivers of the events (Brean et al., 2020; Zheng et al., 2015).

Based on the above discussion, Type A and B events were both collision-limited nucleation. The favorable condition and the banana shape of particle size spectrum for Type A events indicate they were most likely to be the regional events that usually occurred in relatively clean atmosphere (Kanawade et al., 2012). The favorable condition of Type B events was similar to that of Type A, except for the high concentration of $PM_{2.5}$. Part of nucleation mode particles grew into the Aitken mode in Type B events, which was similar to the “suppressed events” defined by Chen et al. (2017). The anthropogenic sources largely influenced Type C events, indicated by the high level of TVOCs. The particles might be generated resulting from the reduced energy barriers (note the slope between $\log J_3$ and $\log[H_2SO_{4,proxy}]$ around 0.5). The high formation rate, low growth rate, and long duration indicated Type C events were like “local events” (Kivekas et al., 2016; Dai et al., 2017).

The particle growth rates (GRs) were calculated for each event day by particle size bin, as summarized in Table 1. The mean growth rates of 10-nm particles were 15.7 ± 9.3 and 17.1 ± 11.5 nm/hr at NJU and NUIST, respectively. Our observations were consistent with another campaign in Beijing (Wang et al., 2013b), in which the GRs were reported to be higher at an urban site (PKU, 4.6 nm/hr) than at a nearby clean site (SDZ, 3.7 nm/hr) in the fall. The abundance of condensable vapor, including sulfuric acid and oxidation products of VOCs, was expected to accelerate particle growth.

The growth of newly formed particles can be partially attributed to condensation of sulfuric acid. We calculated the concentrations of sulfuric acid required for 1 nm/hr growth ($C_{GR=1\text{nm/hr}, H_2SO_4}$) of 10 nm and 40 nm particles with Eq. (4) and estimated the contributions of sulfuric acid in the air to the growth rate of 10 nm and 40 nm particles with Eq. (5). Table S3 summarizes the contribution rates of sulfuric acid to 10 and 40 nm particles (CR_{10} and CR_{40} , respectively). The average CR_{10} for Type A events was 0.25 ± 0.05 and 0.25 ± 0.24 at NJU and NUIST, while that for Type C was 0.39 ± 0.16 and 0.28 ± 0.12 at NJU and NUIST, respectively. The lower CR_{10} for Type A events compared with that for Type C events at both sites implied that other precursors contributed more to particle growth dur-

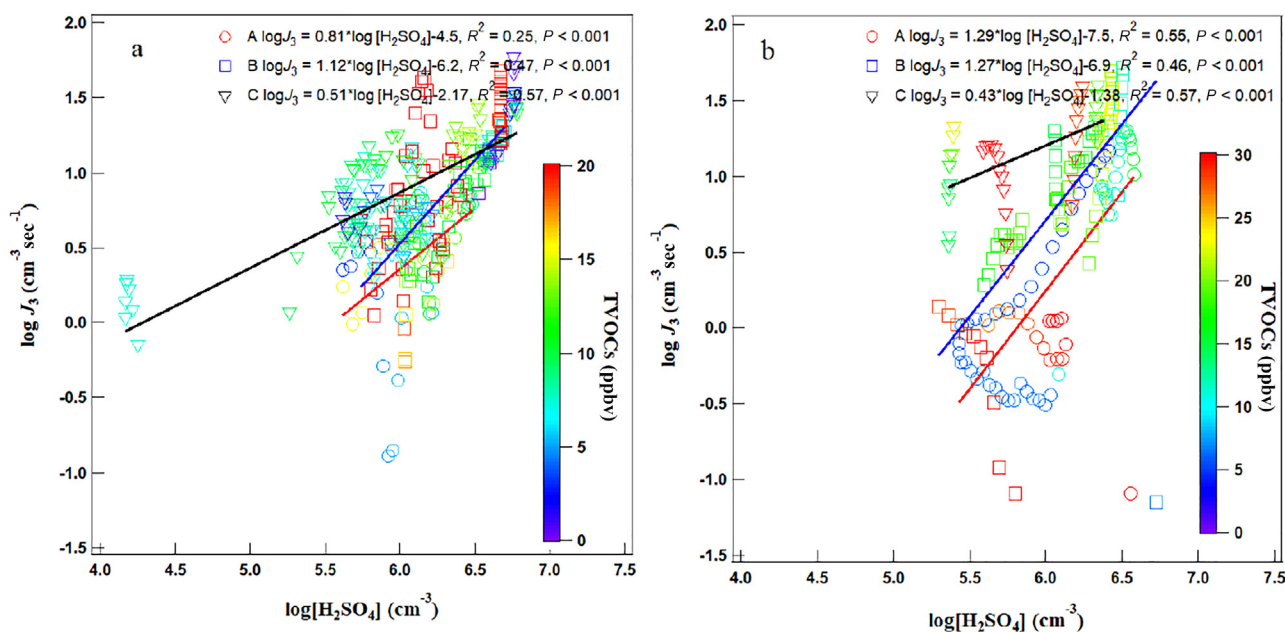


Fig. 6 – Correlations between $\log J_3$ and $\log[\text{H}_2\text{SO}_{4,\text{proxy}}]$ for Type A, B and C events at NJU (a) and NUIST (b). Symbol colors indicate the mixing ratio of TVOCs.

ing a typical NPF event. In contrast, the CR_{40} was smaller for Type C events ($4\% \pm 1\%$ at NJU and $8\% \pm 1\%$ at NUIST) and larger for Type A events ($10\% \pm 2\%$ at NJU and $16\% \pm 2\%$ at NUIST). The CR_{40} was lower than the CR_{10} for all three types of events, suggesting that the growth of 40 nm particles was less influenced by sulfuric acid than that of 10 nm particles.

3. Conclusions

Three types of NPF events were observed based on two campaigns at a suburban and an industrial site in Nanjing. We found that the proportion of Aitken mode particles at the NJU and NUIST sites increased by 13% and 18% during Type A events, respectively, while it did not change significantly during Type B and C events. The results suggest that Type A events contribute significantly to the fine particle concentration in the atmosphere. High solar radiation flux and low RH, temperature, and $\text{PM}_{2.5}$ level were identified as favorable condition for Type A events. The favorable condition of Type B events was similar to Type A, except for the stable high concentration of $\text{PM}_{2.5}$. The favorable meteorological condition of Type C events was opposite to that of Type A. The $\text{PM}_{2.5}$ level of Type C events was higher than that of Type A, with a continuous growth during the daytime. The average J_3 was lowest for Type A events ($7.4 \pm 1.4 \text{ cm}^{-3} \text{ sec}^{-1}$ at NJU and $4.9 \pm 1.9 \text{ cm}^{-3} \text{ sec}^{-1}$ at NUIST) and highest for Type C events ($13.9 \pm 4.5 \text{ cm}^{-3} \text{ sec}^{-1}$ at NJU and $26.7 \pm 12.8 \text{ cm}^{-3} \text{ sec}^{-1}$ at NUSIT). In contrast, the average concentration of sulfuric acid was highest for Type A ($(3.54 \pm 2.56) \times 10^6 \text{ cm}^{-3}$ at NJU and $(2.92 \pm 2.04) \times 10^6 \text{ cm}^{-3}$ at NUSIT) and lowest for Type C ($(1.83 \pm 2.06) \times 10^6 \text{ cm}^{-3}$ at NJU and $(1.67 \pm 1.36) \times 10^6 \text{ cm}^{-3}$ at NUIST). The different slopes of $\log J_3$ vs. $\log[\text{H}_2\text{SO}_{4,\text{proxy}}]$ among event types indicate that collision-limited nucleation was the dominant mechanism for Type A

and B events and that activation nucleation was the dominant mechanism for Type C events. The lowest GR_{10} was found for Type C and the highest for Type A at the both sites. The CR_{10} of sulfuric acid was lowest for Type A events ($25\% \pm 5\%$ at NJU and $25\% \pm 24\%$ at NUIST), implying a larger contribution of other precursors conducive to particle growth in typical NPF events. For aerosol pollution control, therefore, a crucial step is to slow the formation rate of particles by reducing SO_2 emissions, as SO_2 is an important precursor of sulfuric acid. Limiting other gaseous species (e.g., VOCs) could be effective for preventing the ultrafine particles from growing into larger ones.

Acknowledgments

This work was sponsored by the National Natural Science Foundation of China (Nos. 41922052 and 42177080). We would like to thank NOAA for providing the HYSPLIT and TrajStat models.

Appendix A Supplementary data

Supplementary material associated with this article can be found, in the online version, at doi:10.1016/j.jes.2022.07.029.

REFERENCES

- Alonso-Blanco, E., Gomez-Moreno, F.J., Artinano, B., Iglesias-Samitier, S., Juncal-Bello, V., Pineiro-Iglesias, M., et al., 2018. Temporal and spatial variability of atmospheric particle number size distributions across Spain. *Atmos. Environ.* 190, 146–160.

- An, J.L., Wang, H.L., Shen, L.J., Zhu, B., Zou, J.A., Gao, J.H., et al., 2015. Characteristics of new particle formation events in Nanjing, China: Effect of water-soluble ions. *Atmos. Environ.* 108, 32–40.
- An, J.L., Zhu, B., Wang, H.L., Li, Y.Y., Lin, X., Yang, H., 2014. Characteristics and source apportionment of VOCs measured in an industrial area of Nanjing, Yangtze River Delta, China. *Atmos. Environ.* 97, 206–214.
- Anttila, T., Kerminen, V.M., Lehtinen, K.E.J., 2010. Parameterizing the formation rate of new particles: the effect of nuclei self-coagulation. *J. Aerosol. Sci.* 41, 621–636.
- Baalbaki, R., Pikridas, M., Jokinen, T., Laurila, T., Dada, L., Bezantakos, S., et al., 2021. Towards understanding the characteristics of new particle formation in the Eastern Mediterranean. *Atmos. Chem. Phys.* 21, 9223–9251.
- Brean, J., Beddows, D.C.S., Shi, Z.B., Temime-Roussel, B., Marchand, N., Querol, X., Alastuey, A., et al., 2020. Molecular insights into new particle formation in Barcelona, Spain. *Atmos. Chem. Phys.* 20, 10029–10045.
- Cai, M.F., Liang, B.L., Sun, Q.B., Liu, L., Yuan, B., Shao, M., et al., 2021. The important roles of surface tension and growth rate in the contribution of new particle formation (NPF) to cloud condensation nuclei (CCN) number concentration: evidence from field measurements in southern China. *Atmos. Chem. Phys.* 21, 8575–8592.
- Casquero-Vera, J.A., Lyamani, H., Dada, L., Hakala, S., Paasonen, P., Roman, R., et al., 2020. New particle formation at urban and high-altitude remote sites in the south-eastern Iberian Peninsula. *Atmos. Chem. Phys.* 20, 14253–14271.
- Chen, X.M., Virkkula, A., Kerminen, V.M., Manninen, H.E., Busetto, M., Lanconelli, C., et al., 2017. Features in air ions measured by an air ion spectrometer (AIS) at Dome C. *Atmos. Chem. Phys.* 17, 13783–13800.
- Dai, L., Wang, H.L., Zhou, L.Y., An, J.L., Tang, L.L., Lu, C.S., et al., 2017. Regional and local new particle formation events observed in the Yangtze River Delta region. *China. J. Geophys. Res.-Atmos.* 122, 2389–2402.
- Dall'Osto, M., Beddows, D.C.S., Tunved, P., Krejci, R., Strom, J., Hansson, H.C., et al., 2017. Arctic sea ice melt leads to atmospheric new particle formation. *Sci. Rep.* 7, 3318.
- Dal Maso, M., Kulmala, M., Riipinen, I., Wagner, R., Hussein, T., Aalto, P.P., et al., 2005. Formation and growth of fresh atmospheric aerosols: eight years of aerosol size distribution data from SMEAR II, Hyytiälä, Finland. *Boreal Environ. Res.* 10, 323–336.
- Ding, A.J., Fu, C.B., Yang, X.Q., Sun, J.N., Zheng, L.F., Xie, Y.N., et al., 2013a. Ozone and fine particle in the western Yangtze River Delta: an overview of 1 yr data at the SORPES station. *Atmos. Chem. Phys.* 13, 5813–5830.
- Ding, A.J., Wang, T., Fu, C.B., 2013b. Transport characteristics and origins of carbon monoxide and ozone in Hong Kong, South China. *J. Geophys. Res.-Atmos.* 118, 9475–9488.
- Draxler, R.R., and Rolph, G.D., 2010. HYSPLIT (HYbrid single-particle Lagrangian integrated trajectory) model. Available: <http://ready.arl.noaa.gov/HYSPLIT.php>. Accessed September 10, 2021.
- Ezhova, E., Kerminen, V.M., Lehtinen, K.E.J., Kulmala, M., 2018. A simple model for the time evolution of the condensation sink in the atmosphere for intermediate Knudsen numbers. *Atmos. Chem. Phys.* 18, 2431–2442.
- Gao, J., Wang, T., Zhou, X.H., Wu, W.S., Wang, W.X., 2009. Measurement of aerosol number size distributions in the Yangtze River delta in China: formation and growth of particles under polluted conditions. *Atmos. Environ.* 43, 829–836.
- Garmash, O., Rissanen, M.P., Pullinen, I., Schmitt, S., Kausiala, O., Tillmann, R., et al., 2020. Multi-generation OH oxidation as a source for highly oxygenated organic molecules from aromatics. *Atmos. Chem. Phys.* 20, 515–537.
- Gelbard, F., Seinfeld, J.H., 1978. Numerical solution of the dynamic equation for particulate systems. *J. Comput. Phys.* 28, 357–375.
- Größ, J., Hamed, A., Sonntag, A., Spindler, G., Manninen, H.E., Nieminen, T., et al., 2018. Atmospheric new particle formation at the research station Melpitz, Germany: connection with gaseous precursors and meteorological parameters. *Atmos. Chem. Phys.* 18, 1835–1861.
- Hirsikko, A., Bergman, T., Laakso, L., Dal Maso, M., Riipinen, I., Horrak, U., et al., 2007. Identification and classification of the formation of intermediate ions measured in boreal forest. *Atmos. Chem. Phys.* 7, 201–210.
- Hussein, T., Hämeri, K., Aalto, P., Asmi, A., Kakko, L., Kulmala, M., 2004. Particle size characterization and the indoor-to-outdoor relationship of atmospheric aerosols in Helsinki. *Scand. J. Work Environ. Health* 30, 54–62.
- Intra, P., Tippayawong, N., 2007. An overview of aerosol particle sensors for size distribution measurement. *Maejo Int. J. Sci. Technol.* 1, 120–136.
- Kanawade, V.P., Benson, D.R., Lee, S.H., 2012. Statistical analysis of 4-year observations of aerosol sizes in a semi-rural continental environment. *Atmos. Environ.* 59, 30–38.
- Kerminen, V.-M., Pirjola, L., Kulmala, M., 2001. How significantly does coagulation scavenging limit atmospheric particle production? *J. Geophys. Res.-Atmos.* 106, 24119–24125.
- Kivekas, N., Carpman, J., Roldin, P., Leppä, J., O'Connor, E., Kristensson, A., et al., 2016. Coupling an aerosol box model with one-dimensional flow: a tool for understanding observations of new particle formation events. *Tellus B* 68, 29706. doi:10.3402/tellusb.v68.29706.
- Kuang, C., Chen, M., Zhao, J., Smith, J., McMurry, P.H., Wang, J., 2012. Size and time-resolved growth rate measurements of 1 to 5 nm freshly formed atmospheric nuclei. *Atmos. Chem. Phys.* 12, 3573–3589.
- Kulmala, M., 2013. Aerosol formation. *Science* 339 881–881.
- Kulmala, M., Petaja, T., Nieminen, T., Sipila, M., Manninen, H.E., Lehtipalo, K., et al., 2012. Measurement of the nucleation of atmospheric aerosol particles. *Nat. Protoc.* 7, 1651–1667.
- Kurten, A., Bergen, A., Heinritzi, M., Leiminger, M., Lorenz, V., Piel, F., et al., 2016. Observation of new particle formation and measurement of sulfuric acid, ammonia, amines and highly oxidized organic molecules at a rural site in central Germany. *Atmos. Chem. Phys.* 16, 12793–12813.
- Kurten, T., Torpo, L., Ding, C.G., Vehkamäki, H., Sundberg, M.R., Laasonen, K., et al., 2007. A density functional study on water-sulfuric acid-ammonia clusters and implications for atmospheric cluster formation. *J. Geophys. Res.-Atmos.* 112, D04210. doi:10.1029/2006JD007391.
- Lee, H., Lee, K., Lunder, C.R., Krejci, R., Aas, W., Park, J., et al., 2020. Atmospheric new particle formation characteristics in the Arctic as measured at Mount Zeppelin, Svalbard, from 2016 to 2018. *Atmos. Chem. Phys.* 20, 13425–13441.
- Lee, S.H., Gordon, H., Yu, H., Lehtipalo, K., Haley, R., Li, Y.X., et al., 2019. New particle formation in the atmosphere: from molecular clusters to global climate. *J. Geophys. Res.-Atmos.* 124, 7098–7146.
- Lu, Y.Q., Yan, C., Fu, Y.Y., Chen, Y., Liu, Y.L., Yang, G., et al., 2019. A proxy for atmospheric daytime gaseous sulfuric acid concentration in urban Beijing. *Atmos. Chem. Phys.* 19, 1971–1983.
- Mazon, S.B., Riipinen, I., Schultz, D.M., Valtanen, M., Dal Maso, M., Sogacheva, L., et al., 2009. Classifying previously undefined days from eleven years of aerosol-particle-size distribution data from the SMEAR II station, Hyytiälä, Finland. *Atmos. Chem. Phys.* 9, 667–676.

- Merikanto, J., Spracklen, D.V., Mann, G.W., Pickering, S.J., Carslaw, K.S., 2009. Impact of nucleation on global CGN. *Atmos. Chem. Phys.* 9, 8601–8616.
- Metzger, A., Verheggen, B., Dommen, J., Duplissy, J., Prevot, A.S., Weingartner, E., et al., 2010. Evidence for the role of organics in aerosol particle formation under atmospheric conditions. *Proc. Natl. Acad. Sci. U. S. A.* 107, 6646–6651.
- Mikkonen, S., Romakkaniemi, S., Smith, J.N., Korhonen, H., Petaja, T., Plass-Duelmer, C., et al., 2011. A statistical proxy for sulphuric acid concentration. *Atmos. Chem. Phys.* 11, 11319–11334.
- Mirme, A., Tamm, E., Mordas, G., Vana, M., Uin, J., Mirme, S., et al., 2007. A wide-range multi-channel air ion spectrometer. *Boreal Environ. Res.* 12, 247–264.
- Nieminen, T., Lehtinen, K.E.J., Kulmala, M., 2010. Sub-10 nm particle growth by vapor condensation - effects of vapor molecule size and particle thermal speed. *Atmos. Chem. Phys.* 10, 9773–9779.
- Palm, B.B., Campuzano-Jost, P., Day, D.A., Ortega, A.M., Fry, J.L., Brown, S.S., et al., 2017. Secondary organic aerosol formation from in situ OH, O₃, and NO₃ oxidation of ambient forest air in an oxidation flow reactor. *Atmos. Chem. Phys.* 17, 5331–5354.
- Peng, Y., Liu, X.D., Dai, J., Wang, Z., Dong, Z.P., Dong, Y., et al., 2017. Aerosol size distribution and new particle formation events in the suburb of Xi'an, northwest China. *Atmos. Environ.* 153, 194–205.
- Petit, J.E., Favez, O., Albinet, A., Canonaco, F., 2017. A user-friendly tool for comprehensive evaluation of the geographical origins of atmospheric pollution: wind and trajectory analyses. *Environ. Modell. Softw.* 88, 183–187.
- Qi, X.M., Ding, A.J., Nie, W., Petaja, T., Kerminen, V.M., Herrmann, E., et al., 2015. Aerosol size distribution and new particle formation in the western Yangtze River Delta of China: 2 years of measurements at the SORPES station. *Atmos. Chem. Phys.* 15, 12445–12464.
- Salimi, F., Crilley, L.R., Stevanovic, S., Ristovski, Z., Mazaheri, M., He, C., et al., 2015. Insights into the growth of newly formed particles in a subtropical urban environment. *Atmos. Chem. Phys.* 15, 13475–13485.
- Shang, D., Hu, M., Zheng, J., Qin, Y., Du, Z., Li, M., Fang, J., et al., 2018. Particle number size distribution and new particle formation under the influence of biomass burning at a high altitude background site at Mt. Yulong (3410 m), China. *Atmos. Chem. Phys.* 18, 15687–15703.
- Shen, L., Wang, H., Lu, S., Li, L., Yuan, J., Zhang, X., et al., 2016. Observation of aerosol size distribution and new particle formation at a coastal city in the Yangtze River Delta, China. *Sci. Total Environ.* 565, 1175–1184.
- Shen, Y.C., Virkkula, A., Ding, A.J., Wang, J.P., Chi, X.G., Nie, W., et al., 2018. Aerosol optical properties at SORPES in Nanjing, east China. *Atmos. Chem. Phys.* 18, 5265–5292.
- Sihto, S.L., Vuollekoski, H., Leppa, J., Riipinen, I., Kerminen, V.M., Korhonen, H., et al., 2009. Aerosol dynamics simulations on the connection of sulphuric acid and new particle formation. *Atmos. Chem. Phys.* 9, 2933–2947.
- Sipila, M., Berndt, T., Petaja, T., Brus, D., Vanhanen, J., Stratmann, F., et al., 2010. The role of sulfuric acid in atmospheric nucleation. *Science* 327, 1243–1246.
- Vakkari, V., Laakso, H., Kulmala, M., Laaksonen, A., Mamaso, D., Molefe, M., et al., 2011. New particle formation events in semi-clean South African savannah. *Atmos. Chem. Phys.* 11, 3333–3346.
- Vana, M., Komsaare, K., Horrak, U., Mirme, S., Nieminen, T., Kontkanen, J., et al., 2016. Characteristics of new-particle formation at three SMEAR stations. *Boreal Environ. Res.* 21, 345–362.
- Vana, M., Tamm, E., 2002. Propagation of atmospheric aerosol and the area of representativeness of its measurements in the Baltic Sea region. *Atmos. Environ.* 36, 391–401.
- Wang, D.W., Guo, H., Cheung, K., Gan, F.X., 2014a. Observation of nucleation mode particle burst and new particle formation events at an urban site in Hong Kong. *Atmos. Environ.* 99, 196–205.
- Wang, H.L., Zhu, B., Shen, L.J., An, J.L., Yin, Y., Kang, H.Q., 2014b. Number size distribution of aerosols at Mt. Huang and Nanjing in the Yangtze River Delta, China: effects of air masses and characteristics of new particle formation. *Atmos. Res.* 150, 42–56.
- Wang, J., McGraw, R.L., Kuang, C., 2013a. Growth of atmospheric nano-particles by heterogeneous nucleation of organic vapor. *Atmos. Chem. Phys.* 13, 6523–6531.
- Wang, Z.B., Hu, M., Pei, X.Y., Zhang, R.Y., Paasonen, P., Zheng, J., et al., 2015. Connection of organics to atmospheric new particle formation and growth at an urban site of Beijing. *Atmos. Environ.* 103, 7–17.
- Wang, Z.B., Hu, M., Sun, J.Y., Wu, Z.J., Yue, D.L., Shen, X.J., et al., 2013b. Characteristics of regional new particle formation in urban and regional background environments in the North China Plain. *Atmos. Chem. Phys.* 13, 12495–12506.
- Wang, Z.B., Hu, M., Yue, D.L., Zheng, J., Zhang, R.Y., Wiedensohler, A., et al., 2011. Evaluation on the role of sulfuric acid in the mechanisms of new particle formation for Beijing case. *Atmos. Chem. Phys.* 11, 12663–12671.
- Weiden, S.-L.v.d., Drewnick, F., Borrmann, S., 2009. Particle loss calculator – a new software tool for the assessment of the performance of aerosol inlet systems. *Atmos. Meas. Tech.* 2, 479–494.
- Xiao, S., Wang, M.Y., Yao, L., Kulmala, M., Zhou, B., Yang, X., et al., 2015. Strong atmospheric new particle formation in winter in urban Shanghai, China. *Atmos. Chem. Phys.* 15, 1769–1781.
- Yao, L., Garmash, O., Bianchi, F., Zheng, J., Yan, C., Kontkanen, J., et al., 2018. Atmospheric new particle formation from sulfuric acid and amines in a Chinese megacity. *Science* 361, 278–281.
- Ye, Z.L., Liu, J.S., Gu, A.J., Feng, F.F., Liu, Y.H., Bi, C.L., et al., 2017. Chemical characterization of fine particulate matter in Changzhou, China, and source apportionment with offline aerosol mass spectrometry. *Atmos. Chem. Phys.* 17, 2573–2592.
- Yli-Juuti, T., Riipinen, I., Aalto, P.P., Nieminen, T., Maenhaut, W., Janssens, I.A., et al., 2009. Characteristics of new particle formation events and cluster ions at K-puszta, Hungary. *Boreal Environ. Res.* 14, 683–698.
- Yu, H., Ortega, J., Smith, J.N., Guenther, A.B., Kanawade, V.P., You, Y., et al., 2014. New particle formation and growth in an isoprene-dominated ozark forest: from sub-5 nm to CCN-active sizes. *Aerosol Sci. Tech.* 48, 1285–1298.
- Yu, H., Ren, L.L., Huan, X.P., Xie, M.J., He, J., Xiao, H., 2019. Iodine speciation and size distribution in ambient aerosols at a coastal new particle formation hotspot in China. *Atmos. Chem. Phys.* 19, 4025–4039.
- Yu, H., Ren, L.L., Kanawade, V.P., 2017. New particle formation and growth mechanisms in highly polluted environments. *Curr. Pollut. Rep.* 3, 245–253.
- Yu, H., Zhou, L., Dai, L., Shen, W., Dai, W., Zheng, J., et al., 2016. Nucleation and growth of sub-3 nm particles in the polluted urban atmosphere of a megacity in China. *Atmos. Chem. Phys.* 16, 2641–2657.
- Yue, D.L., Hu, M., Zhang, R.Y., Wang, Z.B., Zheng, J., Wu, Z.J., et al., 2010. The roles of sulfuric acid in new particle formation and growth in the megacity of Beijing. *Atmos. Chem. Phys.* 10, 4953–4960.
- Zhang, Q., Jia, S., Yang, L., Krishnan, P., Zhou, S., Shao, M., Wang, X., 2021. New particle formation (NPF) events in China

- urban clusters given by sever composite pollution background. *Chemosphere* 262, 127842.
- Zhang, R., Wang, G., Guo, S., Zamora, M.L., Ying, Q., Lin, Y., et al., 2015. Formation of urban fine particulate matter. *Chem. Rev.* 115, 3803–3855.
- Zheng, J., Ma, Y., Chen, M.D., Zhang, Q., Wang, L., Khalizov, A.F., et al., 2015. Measurement of atmospheric amines and ammonia using the high resolution time-of-flight chemical ionization mass spectrometry. *Atmos. Environ.* 102, 249–259.